Volume 13 | Number 33 | 7 September 2017 | Pages 5493–5614

Soft Matter

rsc.li/soft-matter-journal

ISSN 1744-6848

ROYAL SOCIETY OF CHEMISTRY

PAPER
Hervé Elettro *et al.*
Drop-on-coilable-fibre systems exhibit negative stiffness events and transitions in coiling morphology

Soft Matter

PAPER

Cite this: *Soft Matter*, 2017, **13**, 5509

Drop-on-coilable-fibre systems exhibit negative stiffness events and transitions in coiling morphology†

Hervé Elettro, *[ab] Fritz Vollrath,[c] Arnaud Antkowiak [ad] and Sébastien Neukirch[a]

Received 21st February 2017,
Accepted 9th July 2017

DOI: 10.1039/c7sm00368d

rsc.li/soft-matter-journal

We investigate the mechanics of elastic fibres carrying liquid droplets. In such systems, buckling may localize inside the drop cavity if the fibre is thin enough. This so-called drop-on-coilable-fibre system exhibits a surprising liquid-like response under compression and a solid-like response under tension. Here we analyze this unconventional behavior in further detail and find theoretical, numerical and experimental evidence of negative stiffness events. We find that the first and main negative stiffness regime owes its existence to the transfer of capillary-stored energy into mechanical curvature energy. The following negative stiffness events are associated with changes in the coiling morphology of the fibre. Eventually coiling becomes tightly locked into an ordered phase where liquid and solid deformations coexist.

1 Introduction

In systems where energy has been stored[1] or is continuously supplied,[2] force and deformation may operate in opposite directions, resulting in a so-called negative stiffness. Active biological materials[3] or systems under fluid loading[4] have been shown to exhibit such a behavior. Locally negative stiffness appears as soon as the force–displacement curve of a system in non-monotonic. For example, it is encountered during the buckling of structures in specific geometries such as cylindrical shells,[5,6] beams on elastic foundations,[7] elastic ribbons,[8] or metamaterials.[9]

Here we show that drop-on-coilable-fibre systems also experience regimes of negative stiffness, mainly where capillary-stored energy is transferred into mechanical energy. Drop-on-fibre systems have a long history, from the textile industry[10] to the coating of glass fibres.[11,12] Other examples include the wetting of fibre networks[13] or the influence of capillary forces on elastic deformation of fibres.[14,15] Elastocapillarity,[16] the investigation of the deformation of elastic materials and structures by surface tension, lies at the interface between Physics[17] and Engineering[18] and is used as a way to functionalize and design new systems and materials.[19,20] Recently, taking inspiration from spider-silk fibres, we demonstrated that sufficiently thin fibres can locally buckle and coil within liquid drops (see Fig. 1 and Elettro *et al.*[21]). We further took advantage of the phenomena to design a highly extensible drop-on-coilable-fibre system. In the following we show that in such a system, the active contribution of wetting energy gives rise to a subcritical buckling transition during which the stiffness of the system is negative. We further investigate the consequences of subcriticality and show that it generates hysteresis in the mechanical response of the system (Section 2). Additionally we show that the plateau tension contains coherent

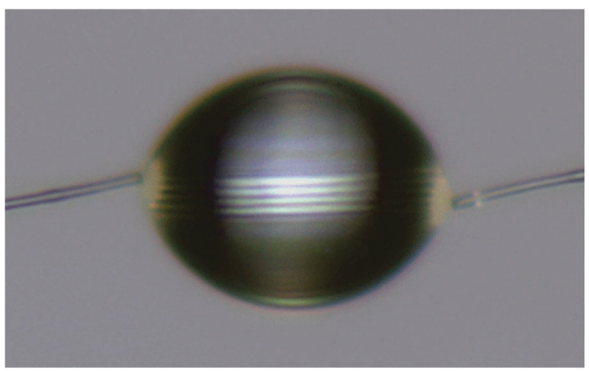

Fig. 1 Thin fibres may buckle and coil inside a liquid drop. A soft thermoplastic polyurethane fibre (Young's modulus E = 17 MPa) with radius r = 2.75 μm is spooled within a silicone oil drop of diameter D = 191 μm.[21]

[a] *Sorbonne Universités, UPMC Univ Paris 06, CNRS, UMR 7190 Institut Jean Le Rond d'Alembert, F-75005 Paris, France*
[b] *Departamento de Física, Universidad de Santiago de Chile, Av. Ecuador 3493, Santiago, Chile. E-mail: herve.elettro@usach.cl*
[c] *Oxford Silk Group, Department of Zoology, University of Oxford, Oxford OX1 3PS, UK*
[d] *Surface du Verre et Interfaces, UMR 125 CNRS/Saint-Gobain, F-93303 Aubervilliers, France*

† Electronic supplementary information (ESI) available: Video of numerical simulations of a drop-on-coilable-fibre system with f_γ = 41, showing the near and far-from-threshold mechanical response and related in-drop coiling rearrangement. See DOI: 10.1039/c7sm00368d

oscillations that consist of alternating regimes of positive and negative stiffness. These regimes are correlated with the drop deformation and the coiling morphology. Packing morphology of a filament in a cavity[22] has been studied as a model for DNA viral capsids.[23,24] Morphogenesis of filaments in flexible cavities is also relevant in several biological systems.[25] Stoop *et al.*[26] studied experimentally and numerically the packing of thin wires in spherical cavities, followed by Vetter *et al.*,[25] who have recently shown that an ordered-to-disordered transition may occur for a filament in an elastic cavity by changing the confinement flexibility.[25,27] Schulman *et al.*[28] investigated the bending of microfibres around liquid droplets, while Roman and Bico[16] studied the deformation of the liquid drop as the rod is wrapping around it with one end free, thus restricting to ordered coiling through the release of twist.[26] Here we show that the packing morphology of the drop-on-coilable-fibre systems changes as the in-drop fibre length is increased and alternates between disordered and ordered.

2 A subcritical buckling transition

Subcritical transitions are discontinuous transitions, as opposed to supercritical transitions where the order parameter grows smoothly from zero. Subcritical transitions are present in a number of fields (*e.g.* Turing bifurcation in reaction–diffusion systems,[29] transition to turbulence[30]). They imply dependence on the loading history, *i.e.* hysteresis. Buckling transitions may be either supercritical or subcritical depending on geometry: buckling of cylindrical shells[5] or ribbons[8] is subcritical (discontinuous), while thin plates and slender beams buckle supercritically.[31] Metabeams may also buckle subcritically due to strong nonlinearities in their mechanical response.[9] In this section we show that drop-on-coilable-fibre systems experience subcritical buckling as part of their unique conformation: in-drop buckling involves both the transfer of wetting energy into mechanical energy and the presence of a non-constant system length, which is reminiscent of beam buckling in sliding sleeves.[32]

As shown by Elettro *et al.*,[21] the drop-on-coilable-fibre system displays a classic solid-like behavior in tension and a remarkable liquid-like behavior in compression. In the solid-like regime (see Fig. 2(a)), the system behaves like a spring, that is, the applied tension T is linearly related to the elongation $|\Delta|$ through the Young's modulus E of the fibre, $T = EA|\Delta|/L$, where A is the area of the cross section of the fibre and L is the length of the fibre in its rest state. In the liquid-like regime (Fig. 2(c)), the system behaves like a soap film, that is, it adapts its length while staying in a state of constant tension $T \approx T_P$ with[21]

$$T_P = F_\gamma - \frac{1}{2}\pi E\frac{r^4}{D^2} \qquad (1)$$

where $F_\gamma = 2\pi r\gamma\cos\theta_Y$ is the meniscus force, γ the liquid–vapor interface energy, θ_Y the contact angle of the liquid on the solid, r the radius of circular cross-section of the fibre, $I = \pi r^4/4$ its second moment of area (EI being the fibre resistance to bending), and D the drop length, measured as the meniscus-to-meniscus distance. For large drops on small fibres, the drop length D is close to the (almost spherical) drop diameter.[11] In the considered range of drop/fibre sizes, the departure from sphericity does not exceed 10% and justifies a spherical drop assumption at first order. Eqn (1) results from an analysis in the moderate post-buckling regime and can be interpreted in terms of energies: per unit length of wetted fibre, the left-hand side is the work of the external applied tension while the right-hand side is the difference between the wetting and the bending energies (coiling being favorable when this difference is positive).

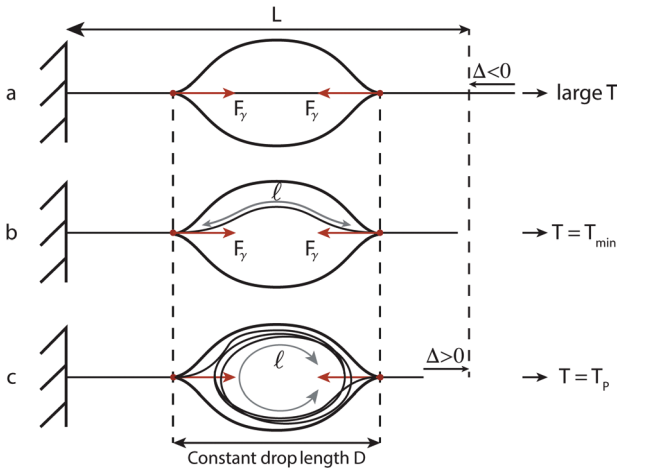

Fig. 2 The subcritical nature of the coiling mechanism derives from the specific mechanics of in-drop capillary buckling. (a) The fibre is under large tension, preventing it from coiling locally. (b) The tension reaches a minimum T_{min} and buckling begins. The drop retains its size D, while swallowing the fibre. (c) The in-drop fibre length ℓ over which coiling occurs increases from D (in case (a)) to $D + \Delta$ (in cases (b) and (c)), which decreases the system resistance.

2.1 Force undershoot during in-drop buckling

We then consider a spherical drop of diameter D resting on a long fibre of length $L \gg D$. For a given capillary force F_γ, a typical in-drop buckling experiment starts with a drop resting on a fibre held taut under large tension T (Fig. 2(a)). As we gradually decrease T, the fibre remains straight until T reaches T_{min} and the portion of the fibre inside the drop buckles (Fig. 2(b)). Inside the drop the fibre is subject to a compressive force $P = F_\gamma - T$, and as tension T is decreased, compression P increases until buckling is reached. The buckling threshold $P_{buck} = F_\gamma - T_{min}$ depends on the capillary force F_γ and detailed calculations yield[33]

$$\sqrt{(F_\gamma - T_{min})\frac{D^2}{EI}} + \sqrt{\frac{T_{min}D^2}{EI}}\tan\left[\frac{1}{2}\sqrt{(F_\gamma - T_{min})\frac{D^2}{EI}}\right] = 0 \quad (2)$$

where we see that the portion of the fibre that buckles has length D, that is buckling tends to be localized inside the drop. We note that for low capillary force F_γ, we have $T_{min} = 0$ as $F_\gamma = \pi^2 EI/D^2$, while for large capillary forces $F_\gamma \gg EI/D^2$ we have $T_{min} \simeq F_\gamma - 4\pi^2 EI/D^2$.

As buckling grows, additional fibre length enters the drop by sliding along the menisci in such a way that the drop length D

(*i.e.* the distance between the two menisci) remains constant. This increase in in-drop fibre length ℓ yields a decrease in bending resistance of the system. We compute the behaviour of the system in this incipient buckling regime. For simplicity reasons, we work under the assumption that the capillary force F_γ is large compared to the bending force EI/D^2, in which case the drop menisci can be viewed as sliding clamps.[33] When a clamped beam of length ℓ is buckling under a compressive force P, it undergoes an end-shortening Δ and in the incipient buckling regime (small Δ/ℓ) we have[34,35]

$$P\ell^2/EI = 4\pi^2 + 2\pi^2\frac{\Delta}{\ell} \quad (3)$$

In the drop-on-fibre experiment (Fig. 2), the compressive force is $P = F_\gamma - T$ and the length of the system under buckling is $\ell = D + \Delta$. Replacing ℓ and developing eqn (3) for small end shortening $\Delta/D \ll 1$ yields

$$\frac{PD^2}{EI} = (F_\gamma - T)\frac{D^2}{EI} \simeq 4\pi^2 - 6\pi^2\frac{\Delta}{D} \quad (4)$$

Eqn (3) and (4) show that while classical buckling is supercritical (positive stiffness $\partial P/\partial\Delta$ in eqn (3)), in-drop buckling is subcritical (negative stiffness $\partial P/\partial\Delta$ in eqn (4)). This change in nature is due to the non-constant fibre length over which buckling occurs. Consequently, as the fibre buckles in the drop (Fig. 2(b)), eqn (4) shows that T is increasing with the end-shortening Δ: the tension is reduced to $T = T_{\min}$ to trigger buckling and is then expected to shoot back upwards after buckling. Eventually the tension stabilizes on the plateau value T_P given by eqn (1), with $T_P > T_{\min}$ (see Fig. 2(c) and 3). The presence of a drop thus modifies the nature of the buckling transition from supercritical (in classic slender beams/fibres) to subcritical (in drop-on-coilable-fibre systems). This behavior is deeply related to the fact that the drop-on-coilable-fibre system is a liquid–solid hybrid: the menisci act as fixed sliding sleeves and force additional fibre to enter the drop, exchanging wetting energy into curvature energy.

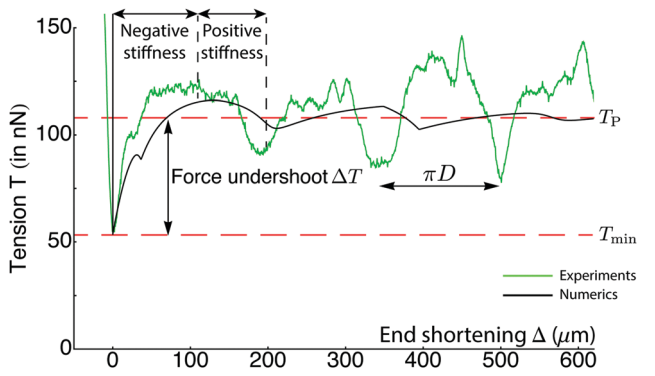

Fig. 3 Drop-on-coilable-fibre systems present alternating regimes of positive and negative stiffness. Comparison between numerical computations (black line) and experimental data (green line) on a TPU/silicone oil system (drop length 62 ± 2 μm, TPU fibre diameter 1.9 ± 0.4 μm and dimensionless capillary force $f_\gamma = 41 \pm 20 > f_\gamma^{th} = \pi^2$, see Section 2.2). The one coil period and the initial negative stiffness regime are well reproduced by the numerical model. Adapted from our previous work in Elettro *et al.*[21]

Several factors may influence the buckling threshold, for example the applied end rotation or the weight of the drop. End rotation is prevented by holding the fibre at one extremity while letting the other end free for a few seconds before attachment, in order to relax twist. The influence of twist, that builds up during fibre coiling, is analyzed in Section 3. The influence of the drop weight M_g is characterized by comparing it to the capillary force F_γ: introducing $C_{\text{grav}} = \frac{M_g}{2F_\gamma}$, we have $C_{\text{grav}} < 2\%$ for drop/fibre sizes used in the present work. The effect of gravity is analyzed in more detail by Elettro.[36]

In Fig. 3, we show an experimental force–displacement curve of a drop-on-coilable-fibre system, along with a comparison with numerical simulations. The numerical simulations model the fibre as an elastic filament, obeying Kirchhoff equilibrium equations.[37] The filament is in interaction with a spherical drop with two compressive point forces at the meniscus locations and a soft-wall barrier potential forbidding exit at any other point. The equilibrium of the system is solved using two-point boundary-value problem techniques (shooting method in Mathematica, and collocation method using the Fortran AUTO code). Note that the weight of the drop and the self-contact of the filament are not taken into account in the model. The numerical simulations only use externally measured parameters (*e.g.* drop length, fibre radius, surface tension) and no fitting parameter. Sensor drifting and force offset during deposition of the drop imply that our experimental force data lack an absolute reference. Consequently we globally adjust it so that the average value of the plateau tension corresponds to eqn (1) (see Materials and methods section). Fig. 3 shows that the model recovers the force undershoot, the presence of negative and positive stiffness intervals, and the periodicity in end-shortening seen in the experiments.

On the one hand, the combination of eqn (1) and (2) yields theoretical values for the force undershoot $\Delta T = T_P - T_{\min}$, and on the other hand it is measured experimentally as the difference between the minimum force and the average value of the plateau tension. This definition of the force undershoot as a relative quantity eludes the problem of sensor drifting exposed above. For each drop/fibre couple, the undershoots are measured three times to ensure reproducibility. We record force–displacement curves for different drop lengths D, and we extract the force undershoot from each curve (see Fig. 4). When the system is subjected to a global compressive force $T < 0$, global buckling occurs if the compression $-T$ exceeds a threshold $\sim EI/L^2$. As L is large, this threshold is indeed very low (piconewtons for centimetric soft microfibres) and we conclude that the drop-on-fibre system is virtually unable to sustain any global compressive force ($T < 0$). Consequently in-drop buckling is not possible as soon as parameters are such that $T_{\min} < 0$. For a given fibre, F_γ is known and positive and a critical drop length D_{ac} can be computed by setting $T_{\min} = 0$ in eqn (2): $D_{\text{ac}} = \pi\sqrt{EI/F_\gamma}$, with drops of length $D < D_{\text{ac}}$ being unable to initiate buckling of the fibre. At $D = D_{\text{ac}}$, $T_{\min} = 0$ and the force undershoot is maximum and equal to the plateau value T_P given by eqn (1) with $F_\gamma = \pi^2 EI/{D_{\text{ac}}}^2$, that is

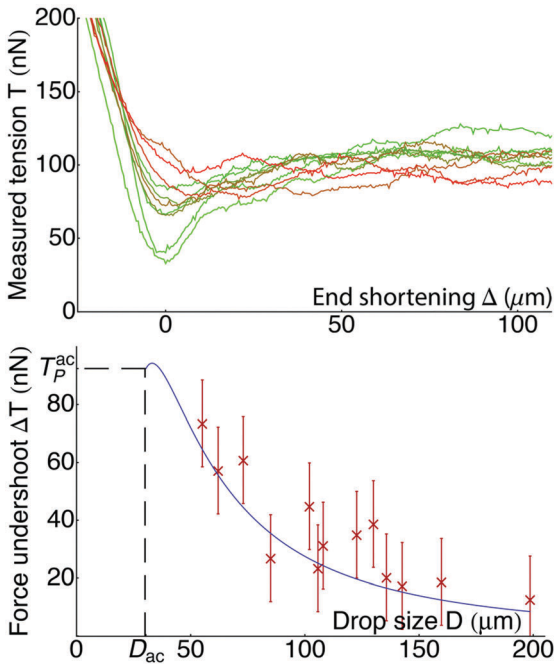

Fig. 4 Top: Force–displacement curves for different drop sizes on a 2 ± 0.4 μm diameter fibre. Colors correspond to dimensionless capillary forces f_γ, from 28 (green) to 236 (red). Bottom: Force undershoot as a function of drop length D for the same fibre. The theoretical prediction, solid line, is in excellent agreement with the experimental data considering the absence of any fitting parameter. The value T_P^{ac} is calculated from eqn (1) with F_γ such that eqn (2) is fulfilled with $T_{min} = 0$: $F_\gamma = \pi^2 EI/D^2$.

$T_P^{ac} = (\pi^2 - 2)EI/{D_{ac}}^2$, or $T_P^{ac} = (1 - 2/\pi^2)F_\gamma$. As D is increased the force undershoot decreases as $1/D^2$. Fig. 4 shows the excellent agreement between the analytical and the experimental values, especially considering the absence of any fitting parameter.

All force measurements shown so far are displacement-controlled experiments. In the following, we shall consider force-controlled experiments. Due to the specific force signature of drop-on-coilable-fibre systems, the two types of experiments lead to different behaviours.

2.2 Mechanical hysteresis

Here we perform experiments where the drop length D is varied. This is equivalent to force-controlled experiments since the dimensionless force $f_\gamma = F_\gamma D^2/EI \propto D^2$ is the control parameter for a given fibre. We consider drop-on-fibre systems held in a very low state of tension $T \ll EI/D^2$, and report the coiling activity as a function of the drop length D. For small D, f_γ is too small to induce coiling but, as drops with increasing D are considered, in-drop buckling is observed as soon as f_γ exceeds π^2 (see eqn (2) with $T_{min} = 0$ and $F_\gamma > 0$), that is we have activation of in-drop coiling if $D > D_{ac}$ with

$$D_{ac} = \sqrt{\frac{\pi^2 Er^3}{8\gamma \cos\theta_Y}} \qquad (5)$$

Experiments with increasing D values are reported in Fig. 5, where the coiling activity is plotted against the drop length D and where

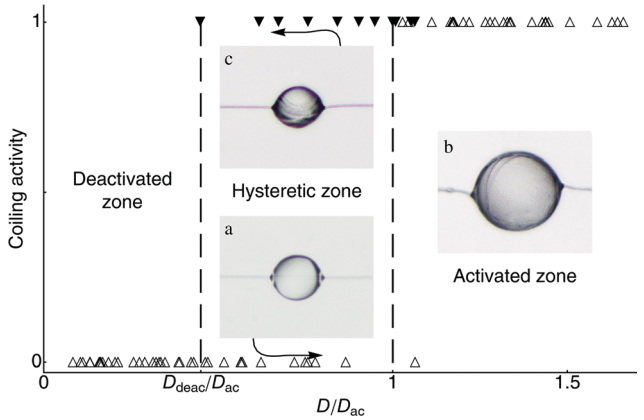

Fig. 5 Coiling activity as a function of the dimensionless drop length $\frac{D}{D_{ac}}\left(=\sqrt{\frac{f_\gamma}{\pi^2}}\right)$. Transitions for activation and deactivation are different, displaying a mechanical hysteresis. Empty triangles represent experiments at increasing drop size while inverted filled triangles are for evaporating drops, decreasing in size. The fibre is made of TPU and measures 5.8 ± 0.4 μm in diameter. The scale is the same in all pictures. Inset (a) shows a drop sitting on a straight fibre, while insets (b) and (c) show a coiled system during evaporation: in (b) the drop size D = 165 μm in length, whereas in (c) D = 103 μm.

we clearly see the activation threshold lying at $D/D_{ac} = 1$. Coiling activity is defined as zero when coiling is not possible and one when it is. Indeed, when the wetting energy overcomes the curvature energy, coiling becomes energetically favorable and will not stop until the drop is filled, a case that has not been reached within our experimental range, even after coiling several cm of fibre in a 100 μm drop. Once activated, the drop-on-coilable-fibre system is in a state of constant tension, the plateau tension T_P being given by eqn (1). For such a coiled system, if we now decrease the drop length D while keeping other parameters fixed, the plateau tension T_P is going to decrease. As the system is virtually unable to sustain any global compressive force ($T < 0$), T_P has to remain positive, and we anticipate a coiling deactivation when $T_P = 0$, that is $D < D_{deac}$ with

$$D_{deac} = \frac{D_{ac}}{\sqrt{\pi^2/2}} = \sqrt{\frac{Er^3}{4\gamma \cos\theta_Y}} \qquad (6)$$

The deactivation drop-length is thus smaller than the activation length by a factor $\frac{\pi}{\sqrt{2}} \simeq 2.2$, resulting in two different thresholds. We experimentally study the deactivation of in-drop buckling by use of evaporation. An ethanol microdrop-laden mist is sent onto a TPU fibre in a confinement chamber. Ethanol drops large enough to induce coiling are deposited on a TPU fibre. After coiling is achieved, the ethanol mist flow rate is slowly decreased, so that drops evaporate in a quasistatic manner. Quasistatic is defined in reference to the timescale for coiling rearrangement, which is here on the order of hundreds of milliseconds. The drop size is recorded optically throughout evaporation.

We thus start with a coiled system in the activated zone $D > D_{ac}$ and let evaporation take place. We observe that coiling remains even when $D < D_{ac}$ (see Fig. 5), but that the drop

envelope strongly deforms and that coiling rearranges to an ordered configuration (see Section 3). The smallest measured coiling diameter is in very good quantitative agreement with the deactivation diameter D_{deac} given in eqn (6). Further evaporation, $D < D_{deac}$, leads to the formation of toroidal coiling held by a liquid film, which eventually snaps and leaves the coiling only bridged by fibre self-adhesion (see Fig. 6). Schulman *et al.*[28] reported similar observations of "dry coils", prepared by winding a polymeric (SIS) fibre on the outer surface of a droplet and then removing the liquid. Further mechanical manipulation of the evaporated sample eventually leads to irreversible uncoiling.

The subcritical nature of the in-drop buckling bifurcation thus leads to two different thresholds for coiling activation and deactivation, and to the manifestation of hysteresis: a system with $D_{deac} < D < D_{ac}$ may be either coiled or not, depending on the loading history.

3 Coiling morphologies and drop deformation

In addition to the essentially flat shape of the plateau, Fig. 3 shows existence of oscillations in the moderate post-buckling regime $\Delta/(\pi D) = O(1)$. These oscillations have smaller amplitude than the initial undershoot peak, and decrease as the capillary force F_γ is increased, to become essentially flat (below sensor resolution) if $F_\gamma > 300EI/D^2$. Moreover they are structured with a period πD for the end-shortening Δ, each cycle corresponding to the addition of one coil inside the drop. Numerical computations[38] show that these cycles come from in-drop rearrangement of the coiling and that 3D and planar configurations alternate, depending on the value of the in-drop fibre length (see also ESI,† video 1). We indeed observe that the typical coiling morphology of a drop-on-coilable-fibre system oscillates between a fully ordered state and a fully disordered state, and both extremes are shown in Fig. 7.

So far the liquid drop has been considered as a rigid sphere. However observations reveal that the drop envelope may undergo strong deformation when interacting with the internal coiling. Hence in the following we consider the packing of a fibre within a deformable liquid drop and study the influence of deformability on the coiling morphology.

Axisymmetry breaking

When the fibre is straight (as in Fig. 1–8) and the fluid is wetting, the drop adopts a well known unduloidal shape

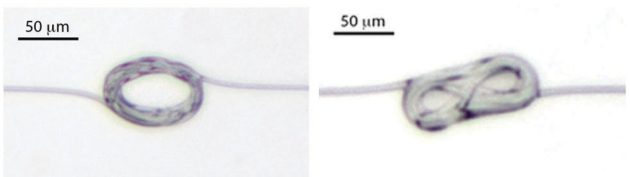

Fig. 6 The evaporation of a droplet containing a coiled fibre leaves highly regular dry coils (left). Residual end rotation may lead to twist instabilities, forming a lemniscate-shaped coil (right).

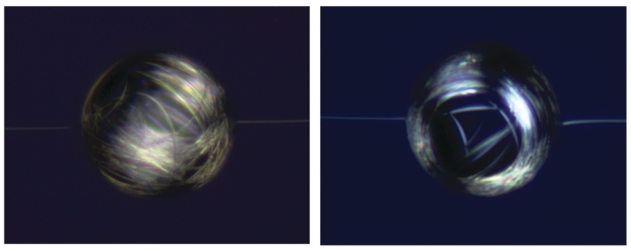

Fig. 7 Polarized light reveals the different coiling morphologies a TPU fibre/silicone oil drop system may adopt: disordered (phase I, left) or ordered (phase II, right). The coiling morphology depends on the precise in-drop fibre length.

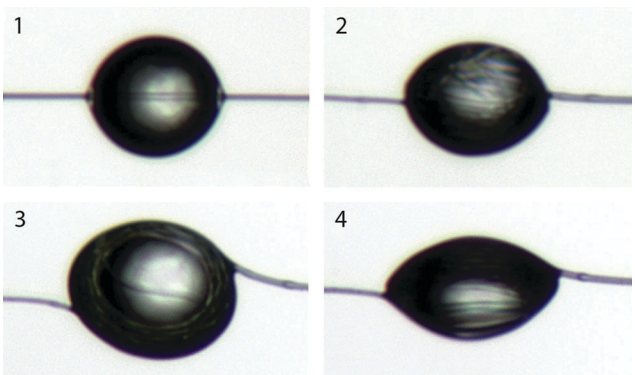

Fig. 8 As the in-drop fibre length increases (from (1) to (4)), the initial axisymmetry of the drop may be broken, resulting in an ellipsoidal shape. Panels (3) and (4) are rotated views of the same drop, illustrating loss of symmetry with respect to the fibre axis. We coin the axisymmetric system (1 and 2) phase I, and the ellipsoidal system (3 and 4) phase II. Here $f_\gamma = 24.7 \pm 5$, $R_0 = 61 \pm 2$ μm and $r = 2.5 \pm 0.4$ μm, and the transition from phase I to phase II occurs near 24 coils. Experimental measures of the drop deformation are reported in Fig. 10.

matching the Young's contact angle in the vicinity of the fibre[11] and is symmetric with respect to the (horizontal) fibre axis for intermediate contact angles. In the presence of coiling, the fibre pushes outwards on the liquid interface with a force F of magnitude $F \propto \frac{\partial}{\partial R}\left(\frac{1}{2}\frac{EI}{R^2}\right) = \frac{EI}{R^3}$ per unit length of fibre. This pressure field is not isotropic and may lead to asymmetric deformation of the liquid interface. Indeed Fig. 8 reveals the change of symmetry axis of the system as more fibre is added in the drop: the initial horizontal axis of symmetry (1) is kept as long as the coiling remains disordered (2). Eventually internal pressure from the fibre is too strong and leads to a deformed drop (3) with an axis of symmetry perpendicular to the horizontal: a localized stretch of the drop envelope represents an opportunity for the in-drop fibre to lower curvature energy. Coiling is then locked in an ordered state as more fibre is added (4).

Quantification of the drop deformation

We consider a drop of initial length $2R_0$ and start increasing the in-drop fibre length ℓ, using the apparent coil number

$n = \frac{\ell}{2\pi R_0}$ as the bifurcation parameter. We quantify the ordering of the coiling with an orientational order parameter S commonly used in the field of liquid crystals[39]

$$S = \langle P_2(\cos\psi)\rangle = \left\langle \frac{3\cos^2[\psi - \langle\psi\rangle] - 1}{2} \right\rangle \quad (7)$$

with $S = 0$ ($S = 1$) corresponding to the fully disordered (ordered) case, and where ψ is the measured angle between the fibre axis at each coil and the initial fibre axis and $\langle\cdot\rangle$ denotes the spatial average. In Fig. 10 we plot $S(n)$ and $\delta R(n)$ where $\delta R(n) = (R(n) - R_0)/R_0$ and $2R(n)$ is the measured maximum drop length, together with the theoretically computed $\delta R_{th}(n)$.

As n is increased from $n = 0$, two different regimes can be identified in the system. For low values of the coil number n (here typically $n \lesssim 20$), coiling is mainly disordered ($S = 0$) except during short ordered intervals ($S = 1$), as underlined by the strong fluctuations of the order parameter during phase I (red curve in Fig. 10). These bursts of ordered coiling have been described in our recent theoretical work.[38] While in phase I, the system keeps its initial horizontal axis of symmetry and we model the liquid interface as a sphere (see Fig. 9-left), whose radius $R(n)$ increases due to the addition of fibre volume. For small δR, conservation of total volume leads to

$$\delta R_I(n) = \frac{R(n) - R_0}{R_0} = \frac{1}{3}\frac{V(n) - V_0}{V_0} = \frac{1}{3}\frac{\pi r^2 \ell}{\frac{4}{3}\pi R_0^3} = \frac{\pi}{2} n \left(\frac{r}{R_0}\right)^2 \quad (8)$$

where r is the fibre radius, ℓ the total in-drop fibre length, $V(n) = (4/3)\pi R^3(n)$ the volume enclosed by the liquid interface, and $n = \frac{\ell}{2\pi R_0}$ the apparent coil number.

As the coil number exceeds a threshold (this threshold is $n^* = 24 \pm 3$ for the system of Fig. 10), the system switches to continuous fully ordered coiling, phase II (see Fig. 3–8). Here n^* is defined experimentally as the center of the transition to constant phase II. We model the liquid interface as two spherical caps of major (minor) axis $2R$ ($2H$) (see Fig. 9-right). The total energy of the system is the sum of the bending energy of the fibre $1/2(EI/R^2)\ell$ and the surface energy of the liquid interface $2\pi\gamma(R^2 + H^2)$. Minimizing this energy with regard to R and H under the constraint of fixed volume $\pi H(R^2 + H^2/3)$,

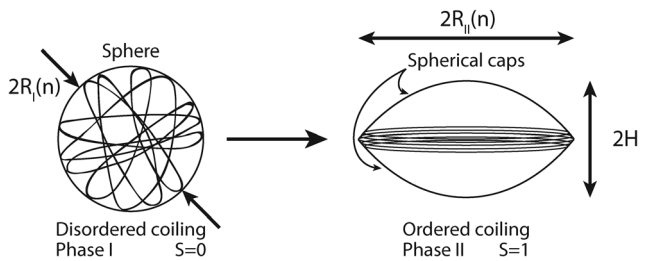

Fig. 9 Spherical cap model of the drop deformed by ordered in-drop fibre coiling. The extreme states are fully disordered coiling in a sphere (phase I, left) and fully ordered coiling in spherical caps (phase II, right).

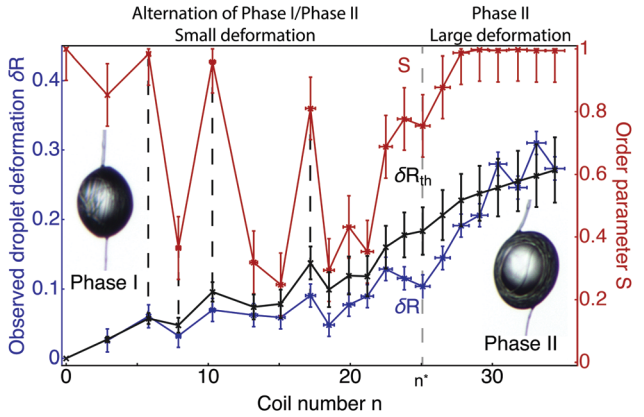

Fig. 10 Comparison between the measured deformation (bottom blue curve) and the theoretical prediction (middle black curve) from eqn (10). The top red curve is the measured order parameter S. Here $f_\gamma = 24.7$, $R_0 = 61 \pm 2$ μm and $r = 2.5 \pm 0.4$ μm. For $n < 22$, coiling alternates between phase I and phase II in a regular manner, well captured by our recent numerical simulations.[38] Drop deformation and coiling rearrangements are strongly correlated, as shown by the corresponding peaks linked by vertical dashed lines. A lock-in transition occurs at $n = 24$, leaving continuous ordered coiling and a highly deformed drop.

we find that for small surface perturbation the deformation of the drop is given by

$$\delta R_{II}(n) = \frac{R - R_0}{R_0} \simeq \frac{n}{4\frac{\gamma R_0^3}{EI} + 3n} \quad (9)$$

We assume that for intermediate coiling morphologies, the drop deformation is the sum of the phase I deformation plus a ratio of the phase II deformation, this ratio being given by the order parameter S. We thus write $\delta R_{th} = \delta R_I + S\cdot\delta R_{II}$. Combining eqn (8) and (9) yields the theoretical drop deformation for any coiling morphology

$$\delta R_{th}(n) = \frac{\pi}{2} n \left(\frac{r}{R_0}\right)^2 + S(n) \times \frac{n}{4\frac{\gamma R_0^3}{EI} + 3n} \quad (10)$$

Eqn (10) is a generalization for any coil number and any order parameter of the results of Roman *et al.*[16]

We tested experimentally eqn (10) for a large number of drop-on-fibre systems. Drop deformation is measured optically as a change of length along the main fibre axis. As the fibre that lies outside the drop is taut throughout our experiments, in-drop fibre length ℓ is measured with the end shortening, $\ell = \Delta$. The order parameter is measured by following optically the direction of each coil when crossing a reference line taken to be the initial fibre axis. Careful repeating of each measurement leads to errors of ± 0.1, although smaller for well defined coiling ($S = 0$ and $S = 1$) as well as for large coiling numbers. For statistical reasons, we restrict to systems with at least $n = 5$ coils. Fig. 10 shows comparison between theory and experiment for a typical measurement. The error bars on the theoretical prediction correspond to the measurement error on the order parameter S, which is an input parameter. The present model

has been tested against several drop-on-coilable-fibre systems where the radius r of the TPU fibre and the initial radius R_0 of the silicone oil drop have been varied. The average difference between theoretical prediction and observed deformation is 15%. Although convenient, the use of a simple setup to assess the order parameter S is quite challenging. This could be improved by the use of X-ray computed tomography, which allows full 3D reconstruction in fine resolution.

We finally remark that the lock-in threshold n^* on the coil number, for which the system enters continuous phase II, could be computed by comparing the energies of both phases. Such a comparison would need an estimation of the twist energy of the system in both phases. Up to now this twist energy has been neglected but we anticipate it to be somewhat different in phases I and II, leading to an energy barrier between the two states. Using a rough estimation of this twist energy barrier as a fraction η of the bending energy (see the Appendix 'Derivation of drop deformation and morphology transition'), we find that the threshold from phase I to phase II should happen at

$$n^* = k(\eta)\frac{\gamma R_0{}^3}{EI} \propto \frac{R_0}{r}\frac{F_\gamma D^2}{EI} \qquad (11)$$

where $k(\eta) \sim O(1)$ is a dimensionless number and $D = 2R_0$. Consequently for systems moderately above the in-drop buckling threshold $F_\gamma = \pi^2 EI/D^2$, the transition to ordered coiling will happen for a coil number of order 10 to 100. In contrast, systems far above the buckling threshold may have their transition to ordered coiling prevented as the system may reach the close-packing limit. Estimating this limit[40] as $n \propto R^2/r^2$, we see that a system where the fibre radius r satisfies $r < r_c \propto \sqrt{\frac{\gamma}{E}R_0}$ will likely not experience the transition to ordered coiling.

4 Conclusion

In conclusion, we showed that the possibility of transferring wetting energy into mechanical energy leads to events of negative stiffness regimes in drop-on-coilable-fibre systems. The consequences include force undershoots in displacement-controlled setups and mechanical hysteresis in force-controlled setups. In both cases, quantitative agreement between experiments, theory and numerics has been reached. We observed that further occurrences of negative stiffness regimes are linked to changes in the coiling morphology, and showed that a lock-in transition may eventually occur, underlining the link between the in-drop fibre length and the drop deformation. Drop-on-coilable-fibre systems thus open new possibilities as complex actuators in light of their unconventional mechanical response. For instance, accurate control may yield new routes to 3D microfabrication and reconfigurable coil-to-cage devices in liquid environments.

Appendix: materials and methods

We prepare microfibres with Thermoplastic PolyUrethane (TPU) from BASF (reference 1185A). We use melt spinning to draw fibres: after TPU pellets are molten on a hot plate at 230 °C, a small amount of liquid TPU is quickly stretched, followed by quenching at room temperature. The obtained fibres have a radius that lies between 1 and 10 μm, depending on the stretching speed. The goal radius is usually achieved within a 2 μm range. The local radius variations are at most by 10% over an extended region of several thousands radii, which corresponds to the typical maximum in-drop fibre length. The fibre and drop diameters are measured optically with a 3 megapixels Leica DFC-295 camera mounted on a Leica macroscope (VZ85RC, 400× zoom, 334 nm per pixel picture resolution) and a remote-controlled micro-step motor. We used either a Phlox 50 × 50 mm backlight (60000 Lux) or an optical fibre with LED lamp (Moritex MHF-M1002) with circular polarizer. The use of polarized light strongly enhances the visibility of the fibre inside of the drop due to birefringence of TPU microfibres. We measured contact angles by superimposing optical images of drops on fibres to corresponding calculated profiles, and found $\theta_Y = 23 \pm 2°$ for the TPU/silicone oil setup and $\theta_Y = 19 \pm 2°$ for the TPU/ethanol setup. We used $\gamma = 21.1$ mN m^{-1} for the silicone oil/air interface and $\gamma = 22.1$ mN m^{-1} for the ethanol/air interface. For evaporation-controlled experiments, we use a megasonic transducer activated at 1.6 MHz (Beijing Ultrasonics) to produce a cloud of micronic droplets, with sizes in the 3–5 μm range (inferred optically) and with controllable outflow. Due to the low intensity of the forces (typically hundreds of nN for our microfibres), we use capacity deflection force sensors (FemtoTools FT-FS100, 5 nN–100 μN range at 20 Hz). While highly sensitive, these sensors have the drawback of drifting slowly with time around 10 nN min^{-1}. This only adds slightly to the measurement errors in rapidly performed tests, typically less than five minutes. In longer tests, the drift can lead to substantial offsets and affect our ability to evaluate absolute force values. Consequently the experimental data in Fig. 3 are offset to match the theoretical value of the plateau tension, given by eqn (1). However, the drift is compensated for graphical purpose only, and does not affect measurements in Fig. 4-bottom, as force undershoots are relative quantities. The force sensor is mounted on a linear micropositioner (SmarAct SLC-1730, repeatability 0.5 μm) and all the tests are displacement-controlled and performed at a quasi-static speed of 12 μm s^{-1}. Young's moduli of the fibres are measured through tensile tests and are found to be 17 ± 2 MPa and do not depend on conditions of preparation. By brushing a fibre with a viscous silicon oil drop (Rhodorsil 47V1000) hanging from a syringe tip, we obtain an array of drops of different sizes. The activation of in-drop buckling is tested by compression of the resulting sample.

Appendix: derivation of drop deformation and morphology transition

We consider the ordered phase II and detail the calculations for the deformation of the drop envelope under the spherical cap model (see Fig. 9). The total potential energy of the system is the sum of the bending energy of the fibre $E_b(R) = 1/2(EI/R^2)\ell$, the twist energy of the fibre E_t, and the surface energy of the two spherical caps $E_S(R,H) = 2\pi\gamma(R^2 + H^2)$. We have a constraint of fixed liquid volume expressed as $(1/3)\pi H(3R^2 + H^2) = (4/3)\pi R_0{}^3$,

where R_0 is the radius of the undeformed spherical drop. As the twist energy E_t is difficult to evaluate we first do not take it into account, and introduce the lagrangian of the system as $\mathscr{L}(R,H) = E_b(R) + E_S(R,H) - \lambda(1/3\pi H[3R^2 + H^2] - 4/3\pi {R_0}^3)$, where λ is the Lagrange multiplier associated to volume conservation. We identify λ as the pressure inside the drop. The equilibrium of the system is then given as a stationary point of $\mathscr{L}$:

$$\frac{\partial \mathscr{L}}{\partial H} = 0 = 4\pi\gamma H - \lambda\pi\left(R^2 + H^2\right) \tag{12a}$$

$$\frac{\partial \mathscr{L}}{\partial R} = 0 = -\frac{EI\ell}{R^3} + 4\pi\gamma R - 2\pi R\lambda H \tag{12b}$$

We work under the assumption that the deformation of the interface is small, that is when R and H are both near R_0 and the pressure λ is near $2\gamma/R_0$. We then write $R = R_0(1 + \varepsilon)$ and $H = R_0 + \varepsilon H_1$ with $|\varepsilon| \ll 1$. Volume conservation yields $H_1 = -R_0$, that is $H = R_0(1 - \varepsilon)$. System (4) is then solved and we obtain $\lambda = (2\gamma/R_0)(1 - \varepsilon)$ and

$$\varepsilon = \frac{\ell EI}{8\pi\gamma {R_0}^4 + 3\ell EI} = \frac{nEI}{4\gamma {R_0}^3 + 3nEI} \tag{13}$$

where we see that for ε to be small, we need the capillary force γR_0 to be large compared to the bending force $EI/{R_0}^2$, and the coil number $n = \ell/(2\pi R_0)$ not to be too large.

We conclude that when the twist energy E_t is neglected, we have a unique equilibrium at $\varepsilon > 0$ (ordered coiling) and no equilibrium at $\varepsilon = 0$ (disordered coiling), but we reckon that taking the twist energy into account might change the situation and stabilize the $\varepsilon = 0$ state. The twist energy is larger in the ordered coiling configuration than in the disordered coiling configuration for the following reason. In the experiments the fibre is held at both extremities, therefore imposing a constraint of zero Link, that is zero end rotation of the ends.[41,42] As a rod deforms in space the Writhe is a real number which measures the circumvolution of the center line in 3D. The more the windings, the higher the Writhe. An estimation of the Writhe is obtained by (i) looking at the rod from a given point of view and projecting the rod shape on a plane perpendicular to the view axis, (ii) counting the number of crossings on the projection, and (iii) starting again with every view axis and averaging the result. The Twist is the integral along the rod of the local twist. An important feature of twisted rod mechanics is that, if both extremities of the rod are held fixed, as the rod deforms in space its Writhe and its Twist change but at all times the sum of the Twist and the Writhe stays constant, equal to the Link.[43] In the disordered coiling configuration we estimate the Writhe to be small due to a statistical balance of positive and negative crossings. Hence the Twist, and therefore the twist energy, has to be small. However in the ordered coiling configuration the Writhe is almost that of a regular spool with n turns, Writhe $\approx n$. We then have Twist $\approx -n$, in order for the sum to be zero. The twist energy of the ordered coiling configuration is then larger than the twist energy of the disordered coiling configuration. It is difficult to be more quantitative without performing complete numerical simulations. Here we simply estimate the difference in twist energy to be equal to a fraction η of the bending energy $E_t^{II} - E_t^{I} \simeq (1/2)\eta(EI/{R_0}^2)\ell$, with $\eta \sim O(0.1)$. This estimation follows from numerical results from Stoop *et al.*[26,38]

We now consider the total potential energy $V = E_b + E_t + E_s$ in both disordered coiling, V^I, and ordered coiling, V^{II}. We evaluate V^I at $R = H = R_0$ and V^{II} at $R = R_0(1 + \varepsilon)$ and $H = R_0(1 - \varepsilon)$ with ε given by eqn (13). We then compute the first order of the difference $V^{II} - V^I$:

$$V^{II} - V^{I} \simeq \frac{2\pi EIn}{R_0}\left(\frac{\eta}{2} - \frac{nEI}{4\gamma {R_0}^3 + 3nEI}\right) \tag{14}$$

For small n, twist energy makes the disordered configuration favorable ($V^{II} - V^I > 0$), but as n reaches a threshold $n^* = \frac{4\eta}{2 - 3\eta}\frac{\gamma {R_0}^3}{EI}$ the ordered configuration becomes favorable ($V^{II} - V^I < 0$).

Acknowledgements

We gratefully thank Natacha Krins, David Grosso, Cédric Boissière, Sinan Haliyo, and Camille Dianoux for helpful discussions. The present work was supported by the French Agence Nationale de la Recherche, grants ANR-09-JCJC-0022-01 and ANR-14-CE07-0023-01, 'La Ville de Paris, Programme Emergence', The U.K. Royal Society, grant IE130506 of the International Exchanges Scheme, the CNRS through a PEPS PTI program, the US Air Force, AFOSR grant FA9550-12-1-0294, the European Research Council, grant SP2-GA-2008-233409, and the Conicyt/Fondecyt post-doctoral fellowship no. 3160152.

References

1 J. Thompson, *Philos. Trans. R. Soc., A*, 1979, **292**, 1–23.
2 R. Lakes, T. Lee, A. Bersie and Y. Wang, *Nature*, 2001, **410**, 565–567.
3 P. Martin, A. Mehta and A. Hudspeth, *Proc. Natl. Acad. Sci. U. S. A.*, 2000, **97**, 12026–12031.
4 J. M. T. Thompson, *Nature*, 1982, **296**, 135–137.
5 S. Timoshenko, *History of strength of materials*, Dover, 1983.
6 G. W. Hunt, *J. Inst. Math. Its Appl.*, 2011, **76**, 2–26.
7 G. W. Hunt, M. K. Wadee and N. Shiacolas, *J. Appl. Mech.*, 1993, **60**, 1033–1038.
8 R. L. Fosdick and E. Fried, *The Mechanics of Ribbons and Möbius Bands*, Springer, 2015.
9 C. Coulais, J. T. Overvelde, L. A. Lubbers, K. Bertoldi and M. van Hecke, *Phys. Rev. Lett.*, 2015, **115**, 044301.
10 N. K. Adam, *J. Soc. Dyers Colour.*, 1937, **53**, 121–129.
11 B. J. Carroll, *J. Colloid Interface Sci.*, 1976, **57**, 488–495.
12 D. Quéré, *Annu. Rev. Fluid Mech.*, 1999, **31**, 347–384.
13 E. Lorenceau, T. Senden and D. Quéré, in *Molecular Gels. Materials with Self-Assembled Fibrillar Networks*, ed. R. Weiss and P. Terech, Springer, 2006, pp. 223–237.
14 A. Sauret, F. Boulogne, K. Somszor, E. Dressaire and H. A. Stone, *Soft Matter*, 2017, **13**, 134–140.

15 C. Duprat, S. Protiere, A. Y. Beebe and H. A. Stone, *Nature*, 2012, **482**, 510–513.
16 B. Roman and J. Bico, *J. Phys.: Condens. Matter*, 2010, **22**, 493101.
17 B. Andreotti, O. Baumchen, F. Boulogne, K. E. Daniels, E. R. Dufresne, H. Perrin, T. Salez, J. H. Snoeijer and R. W. Style, *Soft Matter*, 2016, **12**, 2993–2996.
18 R. Syms, E. Yeatman, V. Bright and G. Whitesides, *J. Microelectromech. Syst.*, 2003, **12**, 387–417.
19 M. Pineirua, J. Bico and B. Roman, *Soft Matter*, 2010, **6**, 4491–4496.
20 T. G. Leong, P. A. Lester, T. L. Koh, E. K. Call and D. H. Gracias, *Langmuir*, 2007, **23**, 8747–8751.
21 H. Elettro, S. Neukirch, F. Vollrath and A. Antkowiak, *Proc. Natl. Acad. Sci. U. S. A.*, 2016, **113**, 6143–6147.
22 E. Bayart, S. Deboeuf, F. Corson, A. Boudaoud and M. Adda-Bedia, *EPL*, 2011, **95**, 34002.
23 P. K. Purohit, J. Kondev and R. Phillips, *Proc. Natl. Acad. Sci. U. S. A.*, 2003, **100**, 3173–3178.
24 A. Leforestier and F. Livolant, *Proc. Natl. Acad. Sci. U. S. A.*, 2009, **106**, 9157–9162.
25 R. Vetter, F. K. Wittel and H. J. Herrmann, *Nat. Commun.*, 2014, **5**, 4437.
26 N. Stoop, J. Najafi, F. K. Wittel, M. Habibi and H. J. Herrmann, *Phys. Rev. Lett.*, 2011, **106**, 214102.
27 R. Vetter, F. K. Wittel and H. J. Herrmann, *EPL*, 2015, **112**, 44003.
28 R. D. Schulman, A. Porat, K. Charlesworth, A. Fortais, T. Salez, E. Raphaël and K. Dalnoki-Veress, *Soft Matter*, 2017, **13**, 720–724.
29 V. Breña Medina and A. Champneys, *Phys. Rev. E: Stat., Nonlinear, Soft Matter Phys.*, 2014, **90**, 032923.
30 C. Godrèche, P. Manneville and B. Castaing, *Hydrodynamics and nonlinear instabilities*, Cambridge University Press, 2005, vol. 3.
31 J. E. Gordon, *Structures: or why things don't fall down*, Da Capo Press, 2003.
32 F. Bosi, D. Misseroni, F. Dal Corso and D. Bigoni, *Proc. R. Soc. A*, 2015, **471**, 20150195.
33 H. Elettro, F. Vollrath, A. Antkowiak and S. Neukirch, *Int. J. Nonlin. Mech.*, 2015, **75**, 59–66.
34 Z. P. Bazant and L. Cedolin, *Stability of Structures: Elastic, Inelastic, Fracture, and Damage Theories*, World Science Publishing, 2010.
35 S. Neukirch, A. Goriely and O. Thomas, *J Sound Vib.*, 2014, **333**, 962–970.
36 H. Elettro, PhD thesis, Université Pierre et Marie Curie, 2015.
37 B. Audoly and Y. Pomeau, *Elasticity and Geometry: From hair curls to the non-linear response of shells*, Oxford University Press, 2010.
38 H. Elettro, P. Grandgeorge and S. Neukirch, *J. Elasticity*, 2016, 1–13.
39 P. De Gennes and J. Prost, *The physics of liquid crystals*, Oxford University Press, 1993.
40 E. Katzav, M. Adda-Bedia and A. Boudaoud, *Proc. Natl. Acad. Sci. U. S. A.*, 2006, **103**, 18900–18904.
41 F. B. Fuller, *Proc. Natl. Acad. Sci. U. S. A.*, 1978, **75**, 3557–3561.
42 G. H. M. van der Heijden, M. A. Peletier and R. Planqué, *Q. Appl. Math.*, 2007, **65**, 385–402.
43 M. Dennis and J. Hannay, *Proc. R. Soc. A*, 2005, **461**, 3245–3254.